EARTH SURFACE PROCESSES AND LANDFORMS
Earth Surf. Process. Landforms **42**, 681–696 (2017)
Copyright © 2016 John Wiley & Sons, Ltd.
Published online 29 September 2016 in Wiley Online Library
(wileyonlinelibrary.com) DOI: 10.1002/esp.4013

Insight into sediment transport processes on saline rangeland hillslopes using three-dimensional soil microtopography changes

Sayjro K. Nouwakpo,[1]* Mark A. Weltz,[2] Kenneth C. McGwire,[3] Jason C. Williams,[4] Al-Hamdan Osama[5] and Colleen H.M. Green[6]
[1] Natural Resources and Environment Sciences, University of Nevada Reno, Reno, NV, USA
[2] Great Basin Rangeland Research Unit, USDA-Agricultural Research Service, Reno, NV, USA
[3] Earth and Ecosystem Sciences, Desert Research Institute, Reno, NV, USA
[4] Southwest Watershed Research Center, USDA-Agricultural Research Service, Tucson, AZ, USA
[5] Department of Civil and Architectural Engineering, Texas A&M University - Kingsville, Kingsville, TX, USA
[6] National Operations Center, USDI-Bureau of Land Management, Denver, CO, USA

Received 23 February 2016; Revised 24 July 2016; Accepted 28 July 2016

*Correspondence to: Sayjro Nouwakpo, Natural Resources and Environment Sciences, University of Nevada Reno, Reno, NV, USA. E-mail: snouwakpo@unr.edu

ESPL
Earth Surface Processes and Landforms

ABSTRACT: In arid and semi-arid rangeland environments, an accurate understanding of runoff generation and sediment transport processes is key to developing effective management actions and addressing ecosystem response to changes. Yet, many primary processes (namely sheet and splash and concentrated flow erosion, as well as deposition) are still poorly understood due to a historic lack of measurement techniques capable of parsing total soil loss into these primary processes. Current knowledge gaps can be addressed by combining traditional erosion and runoff measurement techniques with image-based three-dimensional (3D) soil surface reconstructions. In this study, data (hydrology, erosion and high-resolution surface microtopography changes) from rainfall simulation experiments on 24 plots in saline rangelands communities of the Upper Colorado River Basin were used to improve understanding on various sediment transport processes. A series of surface change metrics were developed to quantify and characterize various erosion and transport processes (e.g. plot-wide versus concentrated flow detachment and deposition) and were related to hydrology and biotic and abiotic land surface characteristics. In general, erosivity controlled detachment and transport processes while factors modulating surface roughness such as vegetation controlled deposition. The extent of the channel network was a positive function of slope, discharge and vegetation. Vegetation may deflect runoff in many flow paths but promoted deposition. From a management perspective, this study suggests that effective runoff soil and salt load reduction strategies should aim to promote deposition of transported sediments rather than reducing detachment which might not be feasible in these resource-limited environments.
Copyright © 2016 John Wiley & Sons, Ltd.

KEYWORDS: soil microtopography; DEM; soil erosion; deposition; sediment transport

Introduction

Hillslope runoff and soil erosion processes play a vital role on rangeland ecosystem sustainability due to their control on resource mobility but they also have significant implications in off-site resource transport. These processes are often the dominant source of sediment in semi-arid systems, accounting for as much as 85% of watershed sediment delivery (Nichols *et al.*, 2013). A good understanding of hillslope processes is therefore crucial to achieve sustainable rangeland management and develop effective mitigation strategies.

In general, physically-based hillslope soil erosion models divide erosion and sediment transport processes into their primary components. For example, the Rangeland Hydrology and Erosion Model (Nearing *et al.*, 2011) recognizes splash and sheet erosion occurring when raindrops impact, detach and transport soil particles in a thin flow and concentrated flow erosion which occurs when runoff collects in deep flow and fluvial erosion and transport processes dominate. In addition to these two processes, there is deposition which occurs when a portion of detached particles never reaches the hillslope outlet but accumulates at specific locations on the eroding surface. Accurate understanding of the magnitude and factors affecting each of these components has significant implications in erosion prediction and mitigation on rangeland. Nevertheless, few methodologies exist that can accurately parse total hillslope sediment production into sheet and splash, concentrated flow and deposition contributions.

Some studies have used multi-scale plot experiments to infer rangeland sediment transport dynamics from differences in erosion and runoff response at different spatial scales (e.g. Wainwright *et al.*, 2000; Bracken and Croke, 2007; Pierson *et al.*, 2011; Williams *et al.*, 2014, 2016). While these techniques can inform well on the spatial and functional connectivity of hillslope processes (Williams *et al.*, 2016), they lack the ability to quantify the explicit magnitude of each process (sheet and splash, concentrated flow, deposition, etc.) at a given spatial scale.

Recent advances in the fields of computer vision and photogrammetry have led to the development of Structure-from-Motion (SfM) photogrammetry, a simple and low-cost alternative to traditional image-based three-dimensional (3D) reconstruction methods. SfM has been successfully used in various geoscience and hydrology applications and is currently viewed as the technology that democratized image-based 3D reconstruction for these disciplines (e.g. Castillo *et al.*, 2012; James and Robson, 2012; Westoby *et al.*, 2012; Nouwakpo *et al.*, 2014). SfM makes possible the routine collection of surface-change information during experimental erosion and hydrology studies and has recently been applied to parse total erosion into elementary processes such as concentrated flow, deposition, and sheet and splash (Nouwakpo *et al.*, 2016a).

The aim of this paper is to gain insight into interaction between hillslope topography, vegetation and sediment transport processes by (1) linking microtopographic dynamics to erosion and sediment transport processes (erosion versus deposition, diffuse versus concentrated flow processes) and (2) relating these processes to runoff, hillslope topography and vegetation. This study was part of a broader research effort aimed at quantifying salt transport from rangelands to the Upper Colorado River head waters. Previous researchers (e.g. Hawkins *et al.*, 1977; Riley *et al.*, 1979; Tuttle and Grauch, 2009) have identified upland areas of the Upper Colorado River Basin (UCRB) in the Mancos Shale and Eagle Valley Evaporite geologic formations as major contributors to the river's salinity. As part of an effort to quantify salt transport from rangelands to UCRB, we conducted experimental rainfall simulation studies in saline rangeland communities in the UCRB. Hydrology, erosion and high resolution surface microtopography changes were routinely measured during these simulations, presenting a unique opportunity to answer many sediment transport questions relevant to these saline rangelands and other sparsely vegetated rangelands.

Material and Methods

Study area

Two sites (Price and Ferron hereafter, Figure 1) in the Mancos Shale geologic formation were selected to conduct rainfall simulation experiments. These sites were selected for their contrasting slope ranges and differences in soil intrinsic properties. The Price site is located near the city of Price, Utah at an elevation of 1649 m. The soil on this site is mapped as a Persayo loam soil series and classified as loamy, mixed, active, calcareous, mesic, shallow typic torriorthents. This soil series is developed from sandstone and shale-derived alluvium. A paralithic shale residuum forms a restrictive layer at depths 0.25 to 0.5 m. This soil is encountered on backslopes of hilly landforms with slopes ranging from 3 to 15%. Measured slopes at the Price site ranged from 0.6 to 10%. The mean annual precipitation at the city of Price for the period 1968–2005 was 239 mm, while average snowfall for the same period was 513 mm (Western Regional Climate Center [WRCC], 2015). Vegetation at the Price site is a shrub-dominated ecosystem comprised of a mix of *Ephedra viridis*, *Atriplex gardneri* and *Achnatherum hymenoides*.

The Ferron site is located near the city of Ferron, Utah at an elevation of 1893 m. The predominant soil type at Ferron is mapped as a complex of Chipeta soil series and Badland areas. The taxonomic classification of the Chipeta soil series is clayey, mixed, active, calcareous, mesic, shallow typic torriorthents. The soil at Ferron is derived from residuum weathered from clayey shale, forming a paralithic restrictive layer at depths 0.1 to 0.5 m. This soil is associated with hilly landforms and is encountered on backslopes ranging from 3 to 35%. Measured slopes at the study area of the Ferron site ranged from 11.4% to 24.5%. Mean annual precipitation and average snowfall measured at Ferron between 1948 and 2005 were respectively 215 mm and 688 mm (WRCC, 2015). Vegetation at Ferron was dominated by *Atriplex corrugata*.

Experimental setup

On each experimental site, a series of rainfall simulations were conducted on 6 m × 2 m erosion plots to quantify sediment and salt transport processes during rainfall-driven erosion processes. Erosion and hydrologic responses were assessed by measuring soil loss, runoff and solute transport under four rainfall intensities corresponding to return periods of 2 (44.1 mm/h), 10 (80 mm/h), 25 (104.4 mm/h) and 50 (135.9 mm/h) years. Intensities were calculated based on the five-minute depth return frequencies published in the National Oceanic and Atmospheric Administration (NOAA) atlas 14 (Bonnin *et al.*, 2006). On each plot, a single rainfall event (Table I) was

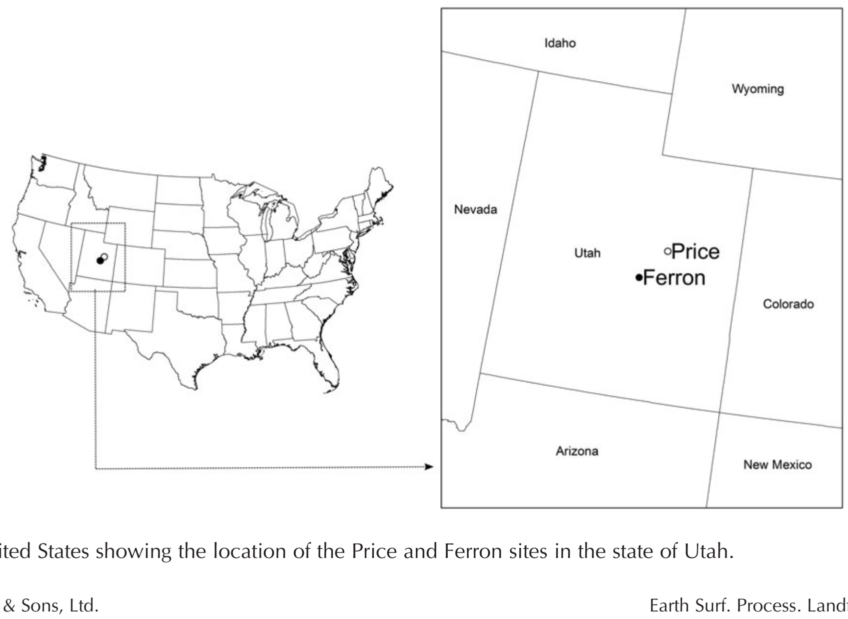

Figure 1. Map of the United States showing the location of the Price and Ferron sites in the state of Utah.

Copyright © 2016 John Wiley & Sons, Ltd.

Table I. Slope, cover characteristic and rainfall intensity applied on each plot.

	Plot ID	P (mm/h)	Veg (%)	Basal (%)	Litter (%)	Rock (%)	SLP (%)
	1	104.4	7.9	0.20	0.7	0.0	5.87
	2	80.0	5.9	0.30	3.2	0.0	4.84
	3	135.9	10.9	0.70	2.0	0.0	0.68
	4	44.1	11.3	1.00	2.9	0.0	5.94
	5	135.9	11.9	0.90	3.2	0.0	6.74
	6	44.1	17.8	2.20	2.4	0.0	5.74
	7	80.0	8.0	1.10	4.1	0.0	6.57
	8	104.4	7.2	1.00	1.7	0.2	10.01
	9	44.1	6.4	0.50	1.4	0.2	9.40
	10	104.4	4.9	0.90	2.0	0.2	7.46
	11	80.0	5.7	1.00	1.5	0.2	3.00
Price	12	135.9	3.3	0.50	1.3	0.3	9.39
	1	80.0	20.6	5.20	4.5	1.0	16.88
	2	44.1	19.8	5.50	3.6	0.7	11.40
	3	104.4	18.0	2.80	2.6	0.5	18.46
	4	135.9	18.3	3.20	3.0	0.2	20.05
	5	44.1	24.0	5.80	3.5	0.0	21.44
	6	135.9	24.2	6.10	5.6	0.0	18.26
	7	104.4	22.3	4.20	2.6	0.0	19.98
	8	135.9	17.7	5.30	2.9	0.2	18.70
	9	104.4	26.4	2.40	2.1	0.3	24.50
	10	80.0	25.2	2.30	3.9	0.0	20.64
	11	80.0	24.3	2.50	2.5	0.0	18.35
Ferron	12	44.1	20.2	2.40	3.1	0.0	18.99

applied to ensure the capture of the dry surface layer which is often high in salt content due to the process of efflorescence (Bowles *et al.*, 1982; Riley *et al.*, 1982). Each rainfall intensity at both sites was replicated three times leading to a total of 12 plots per site.

A Walnut Gulch Rainfall Simulator (WGRS) (Paige *et al.*, 2004) was used in this study (Figure 2a). The WGRS is an oscillating nozzle type simulator with four Veejet 80100 nozzles (Spraying systems, Inc., Wheaton, IL) mounted in-line on a central boom. The effective spray area of this simulator was 6.1 m × 2 m which determined the 6 m × 2 m plot size used in this study. Rainfall intensity is varied in the WGRS from 12 mm/h to 200 mm/h (at 55 kPa nozzle pressure) by modulating oscillation pulse length and nozzle operation timing with a computer-controlled circuitry. As recommended by Paige *et al.* (2004), a nozzle height of 2.44 m was used in this study to approach raindrop energy within the range encountered during natural rainfall events.

At the downslope end of the plot, a runoff collection pan conveyed runoff into a supercritical flume (Figure 2c) where a Teledyne 4230 flow meter (Isco, Inc., Lincoln, NE) measured discharge at a rate of four samples per minute. This automated discharge measurement was validated with periodic manual timed-sampling of runoff rate. Runoff discharge measurements from the Teledyne 4230 were displayed in real-time on a computer screen via a serial communication.

Figure 2. Experimental setup showing (a) rainfall simulator on 6 m × 2 m plot, (b) a close-up view of the camera mount and rail mechanism and (c) the supercritical flume used for runoff discharge measurement and runoff sampling. [Colour figure can be viewed at wileyonlinelibrary.com]

Copyright © 2016 John Wiley & Sons, Ltd.

A rail mechanism mounted lengthwise on the frame of the simulator supported a camera (Figure 2b) which was used to take overlapping pictures before and after each rainfall event. The images were used to reconstruct soil surface microtopography at sub-millimeter resolution. A Canon EOS Rebel T3i (Canon Inc, Tokyo, Japan) equipped with a 20 mm lens was used for acquiring the surface reconstruction pictures. The average camera-ground distance was 2.4 m and the overlap between adjacent pictures 0.15 m. Pictures were taken along two paths 0.76 m apart on either side of the central boom of the simulator. This image network configuration resulted in 80 to 90 pictures to cover each plot. Translucent side curtains on the simulator served the purpose of light diffusers (reducing excessive shadowing in the pictures) and limited the effect of wind on rainfall distribution.

The surface reconstruction procedure relied on control points which were laminated paper targets marked with a checker sign and mounted on an anchor stake. Eight to 10 evenly spaced targets were arranged along the perimeter of each plot. A Nikon NPR 352 total station (Nikon Corporation, Tokyo, Japan) was used to survey control points on each plot for scaling and registering reconstructed soil surfaces.

Experimental protocol

Once a plot was prepared and the simulator set up, a series of pictures were taken before any rainfall to reconstruct soil surface microtopography prior to the event. Rainfall was started immediately after the pre-rain pictures were taken. At the onset of runoff, i.e. when runoff reached the collection pan, the time-to-runoff was recorded. At Price, rainfall was stopped after 15 minutes of runoff had occurred while at Ferron rainfall continued until a trendless real-time hydrograph was observed for 10 minutes, marking steady state conditions. The sampling protocol was modified at Ferron because observation of the hydrographs at Price (where experimentation began) showed that steady state conditions were not consistently attained in all runs. Because these data were also intended to be used for hydrologic modeling, it was important to ensure that steady state was reached during each simulation.

During each rainfall simulation, time-stamped runoff samples were also collected for sediment concentration and water quality analysis. Sampling was done at a frequency of one sample per minute for the first three minutes and every three minutes there on. Sediment concentration samples were collected in 1 l bottles which were immediately weighed to get water and sediment weights and oven-dried at 105 °C to get sediment mass used for concentration calculation. Water quality samples were collected in 60 ml bottles immediately acidified with a hydrochloric acid solution and refrigerated to maintain integrity of the liquid phase chemical speciation. At the end of each rainfall simulation, a delay of 30 minutes was observed before taking post-rain pictures for surface microtopography reconstruction. This delay allowed for ponding water to infiltrate in the soil, for accurate modeling of the soil surface.

Soil surface microtopography was reconstructed using the SfM software Agisoft PhotoScan 1.0 (Agisoft LLC, 2013). The following workflow was followed for each 3D reconstruction: (1) tie points were automatically detected and matched in PhotoScan, (2) a sparse reconstruction was performed by PhotoScan using the matched tie points, (3) control points were manually identified and measured in PhotoScan to scale, register and refine the 3D reconstruction, (4) pre and post sparse reconstructions were aligned in PhotoScan with an affine registration to minimize systematic errors between the two datasets, (5) a dense reconstruction was generated in PhotoScan. Average reconstruction precisions achieved in this study were 3.1 mm and 1.6 mm respectively for the horizontal and vertical directions. Reconstruction precisions were largely limited by the achieved precision in the survey of control points with the total station. For each plot, PhotoScan produced pre-rain and post-rain point clouds which were manually edited to remove vegetation points using the software Cloud Compare (General Public Licence, 2014). Vegetation was removed with the manual segmentation tool in Cloud Compare by manually clipping out areas within the outlines of vegetation. Vegetation-free point clouds were then converted in digital elevation models (DEMs) (Figure 3) at 5 mm resolution and analyzed within ArcGIS (Environmental Systems Research Institute [ESRI], 2011). Sampling the DEMs at 5 mm grid spacing rendered the effect of the 3.1 mm planimetric precision of the reconstruction negligible in the surface change analysis.

Microtopographic analysis

Changes in soil surface microtopography were related to sediment transport mechanisms. Changes to soil surface microtopography were quantified by subtracting post- from pre-rain DEMs, allowing the distinction between erosion areas (negative difference) and deposition areas (positive difference).

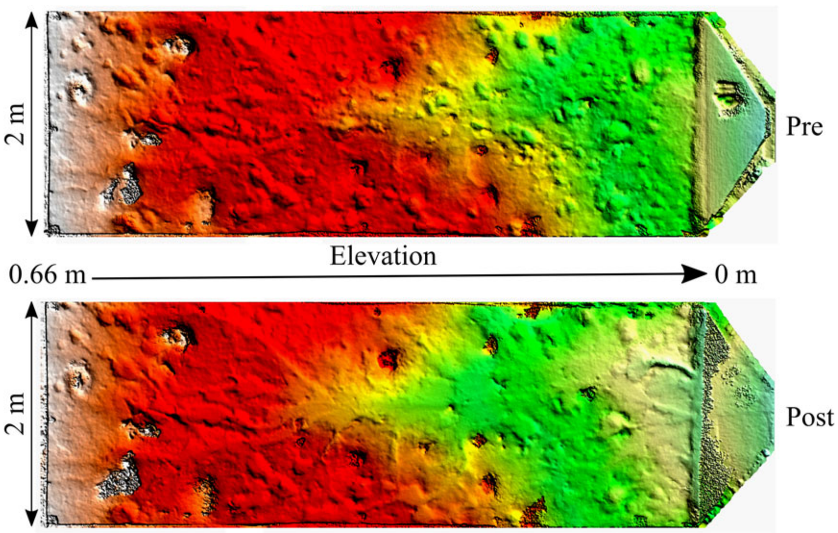

Figure 3. Example of 5 mm resolution digital elevation models (DEMs) representing soil microtopography reconstructed pre- and post-rainfall. [Colour figure can be viewed at wileyonlinelibrary.com]

Copyright © 2016 John Wiley & Sons, Ltd.

To account for increases in elevation due to clay expansion post-wetting, the coefficient of extensibility for the soils at Price and Ferron was measured in the laboratory and found to be 0.034 ± 0.002 across sites. This coefficient was applied to the average wetting front depth after experiment. Measured wetting front depths varied between 4 cm and 8 cm but were more commonly found to be around 5 cm. Therefore a correction of 1.7 mm was subtracted from the post-rain DEM to account for clay expansion. To characterize soil surface response to erosive events, various areal and volumetric surface metrics were calculated from pre- and post-rain DEMs as well as the difference of DEMs. To aid the reader, the nomenclature of these surface change metrics is presented in Figure 4. In addition, one plot at Price ('example plot') was used as an example for illustrative purposes throughout the presentation of surface change metrics in the following sections.

Total erosion, deposition and net loss

The overall spatial extents of erosion processes TAE and deposition TAD were calculated as

$$TAE = n \times A \tag{1}$$

$$TAD = m \times A \tag{2}$$

where n and m are the number of grid cells with respectively negative and positive DEM differences and A is the grid size. On the example plot, TAE and TAD were respectively 9.96 m^2 and 1.36 m^2.

The volumes TVE, TVD and TVN corresponding to erosion and deposition and net loss processes were also quantified as

$$TVE = \sum_{i=0}^{i=n} \Delta Z_i \times A \tag{3}$$

$$TVD = \sum_{j=0}^{i=m} \Delta Z_j \times A \tag{4}$$

$$TVN = TVE - TVD \tag{5}$$

where i and j are respectively grid positions of erosion and deposition and ΔZ is the magnitude of elevation change. On the example plot, TVE and TVD were respectively 0.027 m^3 and 0.003 m^3, resulting in a net erosion TVN of 0.024 m^3.

Erosion and deposition volumes were divided by erosion and deposition extents to obtain the average depths TZE and TZD (in meters). For the example plot, TZE = 0.003 m and TZD = 0.0018 m.

Channel processes

Understanding mechanisms of erosion processes in flow concentration pathways as they relate to other landscape attributes is crucial to accurate soil erosion modeling. In this study, flow concentration pathways were identified by applying the bottom-hat (also known as the black top-hat) mathematical morphology to the original DEMs. The bottom-hat operator detects local extrema in two-dimensional signals such as images and DEMs. This operator has been successfully applied to digital topographic data to delineate flow network and detect erosional incision (e.g. Rodriguez *et al.*, 2002; Schwanghart *et al.*, 2013). The detail presentation of the bottom-hat implementation is beyond the scope of this paper but involved the following steps carried out in ArcGIS:

1. Define a 0.5 m by 0.5 m diamond-shaped kernel as suggested by Hyun-Chong *et al.* (2006).
2. Perform a dilation on the original DEMs (pre and post), by replacing each grid cell value with the maximum elevation within its kernel neighborhood. The resulting maps are the dilated maps.
3. Perform a closing operation by eroding the dilated maps to generate the closed maps. The morphological erosion operation (not to be confused with soil erosion) was done by replacing each dilated grid cell value with the minimum within its kernel neighborhood.
4. The pre- and post-rain bottom-hat maps were then obtained by subtracting the closed maps from the original DEMs. The bottom-hat maps are spatial functions whose minima were areas in the DEMs of local concavities.

Grid cells with bottom-hat values lower than the average of each bottom-hat map were categorized as part of the channel network. Flow networks corresponding to the conditions pre (Net_{pre}) and post (Net_{post}) rain were merged to give a final flow network Net.

The spatial extent of erosion and deposition (CAE and CAD) that occurred within channels were obtained in a similar manner as TAE and TAD.

$$CAE = n_c \times A \tag{6}$$

$$CAD = m_c \times A \tag{7}$$

where n_c and m_c are the number of grid cells with respectively negative and positive DEM differences within Net. Likewise, CVE, CVD and CVN were calculated by applying Equations (3)–(5) to areas within Net. CZE and CZD were also obtained by dividing CVE and CVD by CAE and CAD. On the example plot, out of the 9.96 m^2 of erosion areas, 3.74 m^2 were

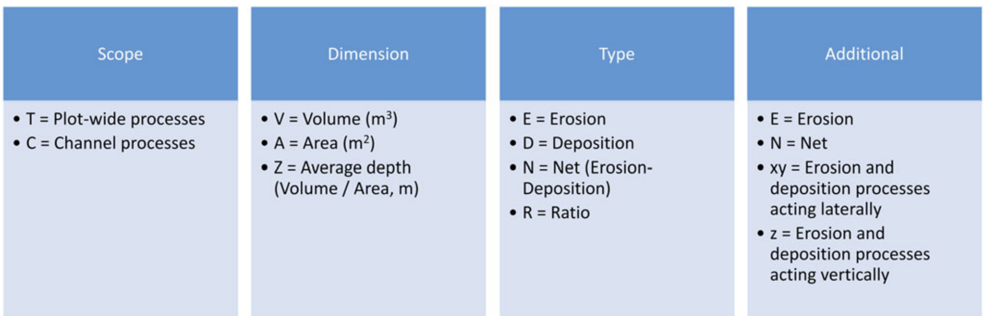

Figure 4. Nomenclature of variables describing surface change. CVE*xy* describes for example volumes of erosion as the result of lateral expansion of the channel network and CAE*xy* is the total area corresponding to this channel lateral expansion. [Colour figure can be viewed at wileyonlinelibrary.com]

Copyright © 2016 John Wiley & Sons, Ltd.

part of the channel network (CAE) likewise, 0.80 m^2 of the deposition areas were part of the channel network (CAD). Erosion and deposition volumes within the channel network CVE and CVD were respectively 0.012 m^3 and 0.002 m^3.

Erosive forces can alter channel networks in both vertical and lateral dimensions depending on hillslope characteristics. These directional changes to the channel network were captured in $Net_{\Delta xy}$ and $Net_{\Delta z}$ for lateral and vertical changes respectively as:

$$Net_{\Delta xy} = Net_{post} \setminus Net_{pre} \quad (8)$$

$$Net_{\Delta z} = Net_{post} \cap Net_{pre} \quad (9)$$

where \ is the set difference operator and ∩ the intersection operator.

From the $Net_{\Delta xy}$ sub-network, spatial and volumetric metrics CAE*xy*, CAD*xy*, CVE*xy*, CVD*xy* and CVN*xy* were calculated whereas $Net_{\Delta z}$ was used to obtain CAE*z*, CAD*z*, CVE*z*, CVD*z* and CVN*z*. Here again, CZE*xy*, CZD*xy*, CZE*z* and CZD*z* were obtained by dividing the respective volumes by the corresponding areas. On the example plot, CAE*xy* and CAD*xy* were respectively 0.58 m^2 and 0.04 m^2 and CVE*xy*, CVD*xy* and CVN*xy* were respectively 0.002 m^3, 9.5×10^{-5} m^3 and 0.002 m^3. CAE*z* is the difference between CAE and CAE*xy* and therefore equals 3.74 m^2–0.58 m^2 = 3.16 m^2. The remaining vertical growth parameters (CAD*z*, CVE*z*, CVD*z* and CVN*z*) were obtained using the same approach.

Other secondary parameters were also calculated:

$$CAR = (CAE + CAD)/(TAE + TAD) \quad (10)$$

$$CVRE = CVE/TVE \quad (11)$$

$$CVRN = CVN/TVN \quad (12)$$

CAR, CVRE and CVRN express the space-based and volume-based ratio of concentrated flow processes that occurred on a plot. For the example plot, CAR = (3.74 + 0.8)/(9.96 + 1.36) = 0.4 and represents the proportion of the plot that belonged to the channel network. CVRE and CVRN were respectively 0.45 and 0.43.

The proportion of concentrated flow energy expenditure in lateral channel expansion versus vertical growth was quantified using two parameters α and α' calculated as:

$$\alpha = CVExy/CVE \quad (13)$$

$$\alpha' = CVNxy/CVN \quad (14)$$

For the example plot, α and α' were 0.21 and 0.23.

Deposition processes were also examined by calculating the proportion of eroded volume that was re-deposited at the plot level (TDR) and in the channels (CDR).

$$TDR = TVD/TVE \quad (15)$$

$$CDR = CVD/CVE \quad (16)$$

For the example plot, TDR = 0.003 m^3/0.027 m^3 = 0.09 and CDR = 0.002 m^3/0.012 m^3 = 0.17. These surface change metrics were related to hydrologic and erosion variables as well as plot slope (SLP) and vegetation (Veg). Hydrologic variables used were precipitation (*P*), runoff discharge at steady state (*Q*), infiltration rate (IR), cumulative runoff (SR) and erosion information were sediment concentration (SC) and total soil loss (SL). Throughout this paper, the units are m^2 for spatial metrics (e.g. TAE, CAE), m^3 for volumetric surface metrics (e.g. TVE, CVE). *P, Q* and IR are in millimeters, SR in 10^{-3} m^3, SC in g/L and *S* is in grams.

The proportion of vegetation cover within each plot was estimated from the high-resolution photogrammetric models by adapting the vegetation removal procedure described in Nouwakpo *et al.* (2016b). Individual 3D points were assessed to determine whether they were part of the vegetation canopy, soil or surface litter using the following method:

1. Create a coarse soil surface topography by superimposing a 5 cm grid over the plot and finding the lowest 3D point within each grid cell.
2. Fit a second-order polynomial trend surface to these local minima.
3. Points that were 20 cm higher than this trend surface were rapidly identified as tall vegetation.
4. Two tests were applied on the remaining points. The slope from each point to its neighbors within 2.5 cm was calculated and the maximum slope within each of four directional quadrants determined. Points with all maximum slopes in a quadrant greater than 20% were labeled as vegetation. The strategy of using the minimum of maximum slope in each direction identified protrusions that were not part of the local trend in surface relief. For the second test, a local height was interpolated at each point from its four nearest neighbors in each directional quadrant using an inverse distance weighing scheme. Points were labeled as vegetation if they were more than 2 cm above the interpolated height.
5. Minor errors of omission where sharp surface features were labeled as vegetation were manually edited.
6. Extracted vegetation point clouds were converted into a two dimensional map by superimposing a 2 mm grid and determining grid cells which contained at least a vegetation point. This fine grid was then resampled to a 60 mm grid, and these coarser cells were labeled as canopy if they contained more than 450 vegetation pixels (half of the 2 mm cells falling in a 60 mm grid). This secondary aggregation helped reduce the effect of over-prediction from labeling a fine-resolution cell as majority-vegetation even if it had just one or two 3D samples within it.

This method of vegetation cover estimation was found to be more accurate than the manual point cloud segmentation with Cloud Compare. The manual point cloud segmentation contained bare ground features within the visually identified outlines of vegetation canopy and this would lead to an overestimation of vegetation cover.

Statistical analysis

To better understand how hillslope topography and vegetation characteristics affect soil erosion and sediment transport processes, multiple regression was performed on each of the surface change metrics described earlier. The premise of this analysis, was that changes to soil microtopography are controlled by four primary factors: hydrologic input, topography, vegetation characteristics and intrinsic soil properties. Explanatory variables were then chosen to represent each of these four

Copyright © 2016 John Wiley & Sons, Ltd.

control variables (Equation (17)). Due to the inherent correlation between many of the explanatory variables, a principal component analysis (PCA) was performed (Figure 5) to select the most dominant variables representing each of the four primary factors. The PCA revealed that the variable Veg controlled most of the variance on the second principal component therefore this parameter was selected to represent vegetation characteristic. Hydrologic input was represented by Q and run duration (Rdur). Topography was captured by slope. To account for differences in intrinsic soil properties and hillslope characteristics between the Price and Ferron sites, a Site factor was added to each regression model. To check for non-linearity in the responses, the regression was repeated on the log-transformed surface change variable (Equation (18)).

$$M = a{\cdot}Q + b{\cdot}Rdur + c{\cdot}SLP + d{\cdot}Veg + SiteFactor + Cste \quad (17)$$

$$Log(M) = a'{\cdot}Q + b'{\cdot}Rdur + c'{\cdot}SLP + d'{\cdot}Veg + SiteFactor' + Cste' \quad (18)$$

where M is a surface change metric described in Equations (1)–(14) and Cste is a constant.

Because slope and vegetation were higher at Ferron than they were at Price, these variables were corrected by subtracting their respective averages at each site from the original values. These transformations improved numerical stability of the least squares procedure which was measured as the Variance Inflation Factors (VIFs). The VIF is commonly used to measure the degree of multi-collinearity with a threshold value of 10 typically used to detect serious multi-collinearity. In this study, VIF values obtained before correcting slope and vegetation varied between 11.6 and 1 but were dramatically reduced to below 2 after these variables were corrected.

A stepwise model selection was performed on each full regression model to select the best-fitting model for a given surface change metric. All statistical analyses were performed in the statistical environment R (R Development Core Team, 2015).

Results

Estimated volume changes as a function of soil loss and runoff

Figures 6 and 7 show the relationship between estimated volume changes with the 3D data and measured cumulative soil loss and runoff. Cumulative soil loss explained 67% of the variability in TVE but was a poor predictor of TVD, explaining only 2% of the variability of this parameter. This decoupling between deposition volume and soil loss resulted in the R^2 of the TVN–SL relationship to be lower (61%) than that of the TVE–SL linear regression. TVN values were also negative in some cases as a result of larger deposition than erosion volumes detected. Factors accounting for these discrepancies include: errors in 3D measurement, changes in density between eroded and deposited sediments and the negligible contribution of soil colloids to microtopography.

Patterns observed between volume change parameters and soil loss held true when cumulative runoff was the explanatory variable (Figure 7). It is also interesting to note from the R^2 values in Figures 6 and 7 that runoff rate performed slightly better than soil loss at predicting microtopographic change. This suggests that runoff discharge may be responsible for some hydrodynamic changes to soil microtopography that have little relation to actual mass of sediment loss.

Plot-wide erosion and deposition processes

Figure 8 shows an example of elevation change map obtained in this study at Ferron and Price. Maps of erosion/deposition patterns for all plots can be found in the Supporting Information. On these maps, one can visually distinguish diffuse processes characterized by low magnitudes of elevation change from concentrated flow processes where larger differences in elevation are observed. Overall, erosion processes (red patterns) dominated each plot with deposition occurring in patchy patterns. One can note on some of the maps some depositional features at the upper boundary of the plot. These depositional features were caused by

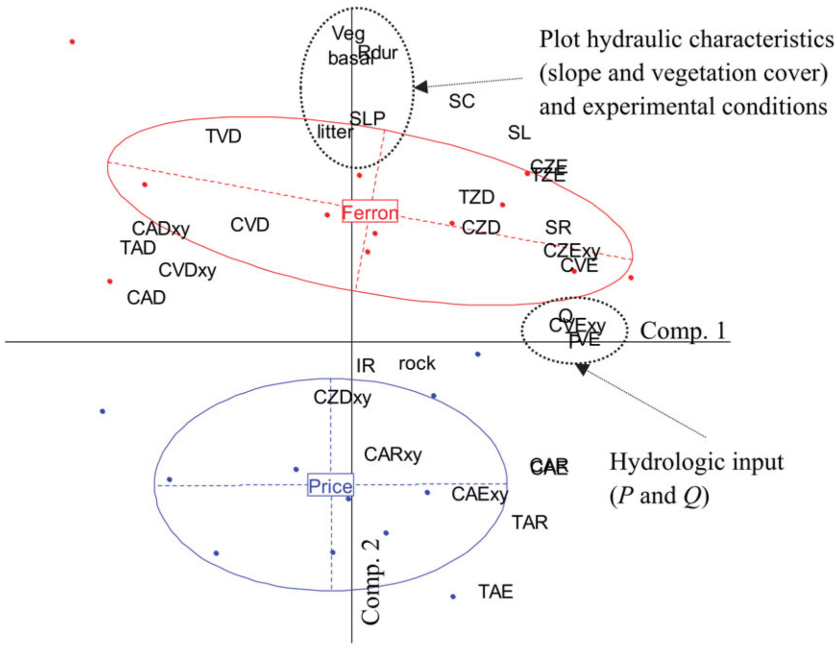

Figure 5. Principal component analysis of the experimental data and surface change metrics. [Colour figure can be viewed at wileyonlinelibrary.com]

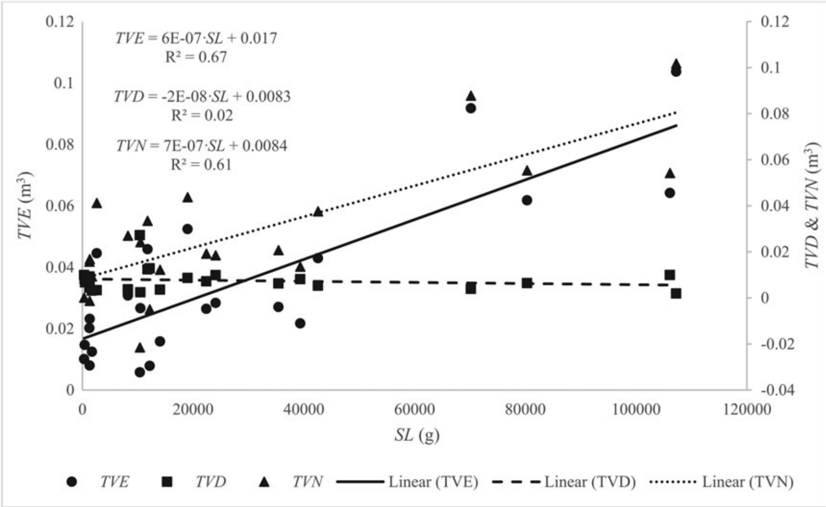

Figure 6. Volume changes as a function of cumulative soil loss. TVE, TVD are volumes (in m^3) of erosion and deposition, TVN is the net volume (in m^3) change (Erosion − Deposition) and SL is the cumulative soil loss (in grams).

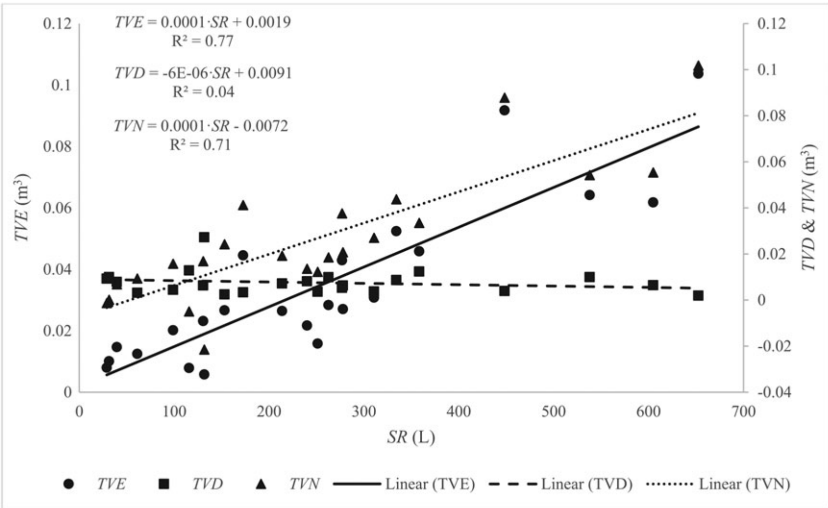

Figure 7. Volume changes as a function of cumulative runoff. TVE, TVD are volumes (in m^3) of erosion and deposition, TVN is the net volume (in m^3) change (Erosion − Deposition) and SR is the cumulative runoff (in liters).

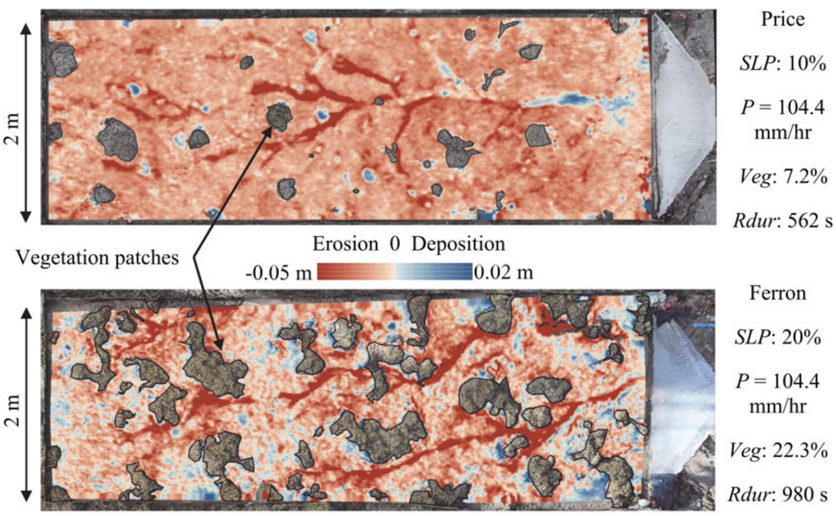

Figure 8. Example of elevation change maps used for the plot-wide analysis. SLP is slope, *P* is rainfall intensity, Veg is vegetation canopy cover, Rdur is rainfall duration in seconds. [Colour figure can be viewed at wileyonlinelibrary.com]

accumulation of splashed material which were not transported downslope due to insufficient flow at the upstream boundary of the plot.

Table II summarizes results of multiple regression analysis performed on the plot-wide surface change metrics. As indicated in the method section, removing the site effect (Price

Copyright © 2016 John Wiley & Sons, Ltd.

Table II. Multiple regression on plot-wide surface change metrics.

	Original					Log-transformed				
Explained variable	Explanatory variables	Coef.	Coef. *p*-value	ANOVA *p*-value	VIF	Explanatory variables	Coef.	Coef. *p*-value	ANOVA *p*-value	VIF
	Intercept	3.89	**3.5E-06**			Intercept	1.28	**2.1E-08**		
	Price	2.93	**1.1E-05**	**3.1E-05**	1.02	Price	0.49	**5.6E-04**	**1.5E-03**	1.02
	Q	0.03	**1.0E-03**	**3.1E-04**	1.07	*Q*	5.3E-03	**2.7E-03**	**2.7E-03**	1.02
TAE $R^2 = 0.76$	Veg	−15.67	0.06	0.08	1.07					
$R^2 = 0.56$*	SLP	0.12	0.18	0.18	1.02					
	Intercept	−9.0E-04	0.90			Intercept	−4.92	**2.8E-19**		
TVE $R^2 = 0.75$	Price	−8.1E-03	0.17	**0.02**	1.02	*Q*	0.02	**6.4E-09**	**6.4E-09**	—
$R^2 = 0.81$*	*Q*	5.5E-04	**3.4E-07**	**3.4E-07**	1.02					
	Intercept	1.6E-03	0.05			Intercept	−6.22	**3.1E-22**		
	Price	−2.5E-03	**1.1E-03**	**1.0E-04**	1.02	Price	−0.49	**2.0E-05**	**8.2E-07**	1.02
	Q	6.0E-05	**5.0E-07**	**5.0E-07**	1.02	*Q*	0.01	**1.0E-09**	**1.3E-09**	1.04
TZE $R^2 = 0.79$						Rdur	2.5E-04	0.06	0.07	1.02
$R^2 = 0.91$*						SLP	0.02	0.15	0.15	1.00
	Intercept	5.15	**1.6E-08**			Intercept	1.67	**2.2E-07**		
	Price	−0.94	0.06	0.19	1.02	Price	−0.24	0.18	0.49	1.02
	Q	−0.03	**6.5E-05**	**6.5E-05**	1.02	*Q*	−0.01	**8.1E-05**	**3.3E-05**	1.07
TAD $R^2 = 0.61$	SLP	−0.12	0.15	0.15	1.00	Veg	3.51	0.21	0.32	1.07
$R^2 = 0.66$*						SLP	−0.06	0.08	0.08	1.02
	Intercept	0.01	**1.0E-04**			Intercept	−4.62	**5.5E-13**		
	Price	−3.4E-03	0.11	0.15	1.02	Price	−0.39	0.08	0.11	1.02
	Q	−3.9E-05	0.16	0.11	1.04	*Q*	−3.6E-03	0.21	0.07	1.07
TVD $R^2 = 0.27$	Rdur	4.3E-06	0.17	0.17	1.02	Veg	8.29	**0.02**	**0.04**	1.07
$R^2 = 0.45$*						SLP	−0.07	0.08	0.08	1.02
	Intercept	1.3E-03	**4.1E-03**			Intercept	−6.38	**2.5E-21**		
	Q	2.8E-05	**2.6E-05**	**9.1E-05**	1.07	*Q*	8.0E-03	**2.7E-04**	**6.3E-04**	1.05
TZD $R^2 = 0.63$	Rdur	9.0E-07	0.13	0.14	1.02	Veg	4.69	**0.04**	**0.04**	1.05
$R^2 = 0.51$*	Veg	0.01	**0.02**	**0.02**	1.05					
	Intercept	−0.02	**0.03**			Intercept	−5.89	**4.0E-10**	**0.0E + 00**	
	Q	6.0E-04	**6.0E-07**	**6.0E-07**	—	*Q*	0.02	**1.5E-04**	**3.1E-05**	1.15
TVN $R^2 = 0.70$						Veg	−15.12	**0.01**	**0.01**	1.09
$R^2 = 0.73$*						SLP	0.13	0.11	0.11	1.06
	Intercept	1.63	**1.2E-03**			Intercept	0.06	0.87		
	Price	−0.59	0.12	0.20	1.02	*Q*	−0.02	**1.1E-04**	**3.9E-05**	1.05
TDR $R^2 = 0.36$	*Q*	−0.01	**0.02**	**0.02**	1.04	Veg	8.62	0.11	0.17	1.07
$R^2 = 0.64$*	Rdur	7.1E-04	0.19	0.19	1.02	SLP	−0.10	0.10	0.10	1.02

Note: All variables were calculated from microtopographic data of the entire plot surface. TAE and TAD are areal extents (in m^2) of erosion and deposition; TVE, TVD are volumes (in m^3) of erosion and deposition and TVN is the net volume (in m^3) change (Erosion − Deposition); TZE and TZD are average depths (in meters) of erosion and deposition; TDR is the ratio of deposition over erosion volumes (TVD/TVE). R^2 values for log-transformed explained variables are marked with an asterisk (*). Values in bold font highlight statistical significance at a 5% confidence level.

versus Ferron) from the explanatory variables Veg and SLP improved the numerical reliability of the estimated regression coefficients and this is illustrated by the low VIF values (< 2). A statistical significance level of 5% was used in this paper to determine the effect of an explanatory variable on surface change metric.

The spatial extent of erosion TAE was on average 2.93 m^2 higher at Price than it was at Ferron and this might be due to the fact that vegetation is sparser on the former site, leading to more exposed soil surface for erosion. It is also important to note the negative effect of Veg on TAE albeit only significant at a 10% confidence level which further supports this theory of greater soil surface exposure in the higher TAE at Price. Runoff discharge showed a significant increasing effect on TAE.

The analysis on the original volumes TVE showed that plots at Price underwent 0.01 m^3 less detachment than at Ferron, likely the result of several factors including slope, run duration and possibly differences in soil erodibility between both sites. Steeper slopes at Ferron resulted in higher erosion rates at this site compared to Price. Longer run durations at Ferron could also explain the larger erosion volumes at this site. This result highlights the importance of slope as a detachment driver since the greater soil surface exposure at Price was effectively compensated by the low slopes at this site. Here again, runoff discharge plays a statistically significant increasing effect on erosion volumes. The log-transformation resulted in an improvement of the R^2 of the regression on TVE but with reduced sensitivity to the site effect.

Our results on TAE and TVE, suggest that erosion volumes were significantly lower at Price but with larger exposed surfaces. This is confirmed in the significantly lower average erosion depth observed at this site compared to Ferron ($TZE_{Price} = TZE_{Ferron} - 2.5$ mm). The analysis also shows a significant and positive effect of runoff discharge on erosion depth. Applying the log-transformation revealed the effects of run duration and slope on TZE but these effects were not statistically significant at 5% confidence level. Both runoff duration and slope had positive effect on TZE with runoff duration statistically significant at 10% and slope at 20%.

Deposition extent TAD showed only a significant effect (negative) of runoff discharge. Unlike what was observed on TAE, the extents of deposition were not statistically different between sites. These results suggest that runoff discharge controlled the spatial extent of areas undergoing active erosion. Since in this study, TAD was the complement of TAE on the fixed-boundary plot (assuming minor influence of the excluded vegetation

Copyright © 2016 John Wiley & Sons, Ltd.

patches), a positive effect of Q on TAE would most likely result in a negative effect of this variable on TAD. It is also worth noting the negative effect (at 10% confidence level) of slope on deposition extent. Deposition volumes TVD related non-linearly (log-transformation) with vegetation. Vegetation promoted deposition within the plots.

It is also interesting to note the reduced significance of the effect of discharge on TVD compared to that observed on TAD, suggesting that a decreasing effect of discharge might be present but dominated by that of vegetation. The decreasing effect of slope was also present on TVD at 10% confidence level. These results suggest that while reducing erosivity (by controlling runoff and slope) might promote deposition, more sensible results can be achieved by increasing overall surface hydraulic roughness through biotic factors such as vegetation or other abiotic factors. In this study, runoff discharge represents the erosivity of both rainfall (splash detachment) and concentrated flow (hydraulic detachment) because rainfall intensity and runoff discharge were highly correlated ($R^2 = 0.93$) with an average runoff coefficient of 0.74.

The average depth of deposition TZD showed statistically significant positive effects of discharge and vegetation. The positive effect of discharge here can be explained by spatial constraint theory with a significant reduction of areas available for deposition (TAD–Q relationship) while the volumes of deposition were weakly impacted. In other words, everything else being equal, an increase in discharge resulted in the same amount of deposition occurring on a smaller area, resulting in a thicker deposition layer.

Channel processes

Figure 9 shows an example of elevation change map obtained in the delineated channel network. Maps of the 24 plots are available as Supporting Information. Overall, elevation changes in channel areas were greater in magnitude than their surroundings, suggesting that the bottom-hat operator effectively delineated areas of flow concentration where flow depth and erosive power were high. The average depth of erosion within the delineated channel network (CZE) was 3.5 mm at Price and 7.6 mm at Ferron while plot-wide erosion depths, TZE were respectively 3 mm and 3.5 mm.

Tables III and IV summarize results from the multiple regression analysis on surface change metrics within the channel network. Unlike the plot-wide analysis, the extent of erosion within the channel network CAE did not show any statistically significant difference between sites, leaving only discharge as the main variable promoting CAE. Plot-wide erosion extent was site-dependent likely because of the difference in vegetation cover and slope between both sites. An increasing effect of slope on CAE was also detected but only significant at a 10% level.

Channel erosion volumes CVE were non-linearly dependent on both discharge and site with lower volumes at Price. The most likely factor explaining these lower concentrated flow detachment volumes at Price is the fact that slopes were shallower at this site compared to Ferron, resulting in lower detachment energy. This is further supported by the positive effect (significant at 10%) of the variable SLP on log(CVE). The average depth of erosion within the channel network CZE showed a non-linear behavior with statistically significant increasing effects of Q and Rdur and lower CZE at Price. It is also important to note the increasing effect of SLP on CZE significant at a 10% level. These results suggest that channel networks at Price and Ferron were similar in extent, but the intensity of concentrated flow erosion was significantly higher at Ferron owing to the steeper slopes and the longer run duration at this site.

To show the effect of concentrated flow processes on sediment concentration, a multiple regression analysis was performed on SC using Site, Q, SLP, CZE and CZD (Equation (19)).

$$SC = 100.26 + \left| \begin{array}{l} -82.26 \text{ for Price} \\ 0 \text{ Otherwise} \end{array} \right. + 4.87SLP + 0.87Q - 2592CZE - 9163CZD, \ R^2 = 0.91 \quad (19)$$

The p-values of the coefficients are 6.5×10^{-7} for the intercept, 6.4×10^{-7} for Site, 0.003 for SLP, 6.4×10^{-4} for Q, 0.30 for CZE and 0.02 for CZD. Sediment concentration was lower at Price and positively impacted by slope and discharge. In addition, the p-value of the CZE coefficient was substantially greater than 0.05, suggesting that this variable had no statistically significant effect on sediment concentration. CZD had however a significant and negative effect on sediment concentration. The absence of effect of CZE on sediment concentration can be explained by the fact that slope and discharge in Equation (19) already captured most of the effect inherent to detachment processes. When CZE and CZD are replaced by their plot-

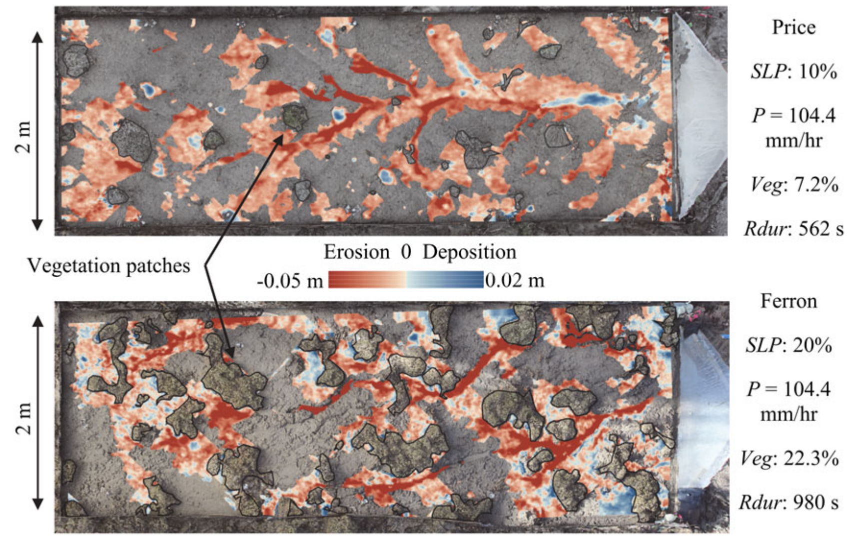

Figure 9. Example of elevation change maps used for the analysis of channel processes. SLP is slope, P is rainfall intensity, Veg is vegetation canopy cover, Rdur is rainfall duration in seconds. [Colour figure can be viewed at wileyonlinelibrary.com]

Copyright © 2016 John Wiley & Sons, Ltd.

Table III. Multiple regression analysis on channel processes.

	Original					Log-transformed				
Explained variable	Explanatory variables	Coef.	Coef. *p*-value	ANOVA *p*-value	VIF	Explanatory variables	Coef.	Coef. *p*-value	ANOVA *p*-value	VIF
	Intercept	1.69	**3.8E-06**			Intercept	0.47	**1.9E-03**		
	Price	0.31	0.16	0.44	1.02	Price	0.16	0.15	0.37	1.02
	Q	0.01	**1.2E-04**	**4.7E-05**	1.07	*Q*	6.1E-03	**3.4E-04**	**3.4E-04**	1.02
CAE $R^2 = 0.66$	Veg	−4.97	0.15	0.25	1.07	SLP	0.03	0.20	0.20	1.00
$R^2 = 0.53$	SLP	0.08	0.06	0.06	1.02					
	Intercept	1.4E-03	0.70			Intercept	−5.49	**5.5E-19**		
	Price	−9.8E-03	**4.8E-03**	**4.5E-04**	1.02	Price	−0.40	**5.7E-03**	**1.7E-04**	1.02
CVE $R^2 = 0.78$	*Q*	2.9E-04	**4.1E-07**	**4.1E-07**	1.02	*Q*	0.02	**8.2E-10**	**8.2E-10**	1.02
$R^2 = 0.89$						SLP	0.05	0.05	0.05	1.00
	Intercept	2.3E-03	**0.02**			Intercept	−5.98	**6.9E-24**		
	Price	−3.3E-03	**2.2E-04**	**2.1E-05**	1.02	Price	−0.56	**1.3E-07**	**5.0E-09**	1.02
	Q	7.0E-05	**4.0E-07**	**4.0E-07**	1.02	*Q*	0.01	**2.4E-11**	**3.1E-11**	1.04
CZE $R^2 = 0.81$						Rdur	2.5E-04	**0.02**	**0.02**	1.02
$R^2 = 0.95$						SLP	0.02	0.07	0.07	1.00
	Intercept	2.00	**1.6E-08**			Intercept	0.71	**2.0E-04**		
	Q	−1.0E-02	**1.4E-03**	**4.9E-04**	1.05	*Q*	−8.2E-03	**4.3E-04**	**1.2E-04**	1.05
CAD $R^2 = 0.55$	Veg	5.23	0.12	0.19	1.07	Veg	4.75	0.06	0.10	1.07
$R^2 = 0.62$	SLP	−0.07	0.08	0.08	1.02	SLP	−0.06	**0.04**	**0.04**	1.02
	Intercept	4.7E-03	**2.8E-08**			Intercept	−5.52	**3.7E-23**		
	Rdur	2.7E-06	0.10	0.09	1.00	Veg	9.51	**7.0E-03**	**0.01**	1.02
CVD $R^2 = 0.35$	Veg	0.04	**0.04**	0.06	1.02	SLP	−0.07	0.07	0.07	1.02
$R^2 = 0.36$	SLP	−3.3E-04	0.10	0.10	1.02					
	Intercept	1.7E-03	**5.8E-04**			Intercept	−6.17	**3.0E-22**		
	Q	2.9E-05	**2.8E-05**	**1.2E-04**	1.07	*Q*	7.2E-03	**6.5E-05**	**2.7E-04**	1.07
CZD $R^2 = 0.64$	Rdur	1.0E-06	0.09	0.11	1.02	Rdur	2.8E-04	0.09	0.10	1.02
$R^2 = 0.61$	Veg	0.02	**0.01**	**0.01**	1.05	Veg	4.34	**0.02**	**0.02**	1.05
	Intercept	−2.6E-03	0.58			Intercept	−5.64	**2.8E-09**		
	Price	−1.0E-02	**0.02**	**2.7E-03**	1.02	Price	−0.96	**8.7E-04**	**4.9E-05**	1.20
	Q	2.8E-04	**1.9E-05**	**7.5E-06**	1.07	*Q*	0.02	**1.8E-04**	**6.5E-04**	1.30
	Veg	−0.08	0.17	0.23	1.07	Rdur	4.5E-04	0.16	0.38	1.07
CVN $R^2 = 0.75$	SLP	9.5E-04	0.18	0.18	1.02	Veg	−7.69	0.06	0.10	1.10
$R^2 = 0.86$						SLP	0.13	**0.01**	**0.01**	1.20
	Intercept	0.43	**4.8E-16**			Intercept	−0.86	**6.6E-15**		
	Price	−0.07	**7.0E-05**	**2.6E-05**	1.02	Price	−0.17	**6.9E-05**	**2.5E-05**	1.02
CAR $R^2 = 0.69$	*Q*	5.4E-04	**8.7E-03**	**0.02**	1.07	*Q*	1.3E-03	**7.8E-03**	**0.02**	1.07
$R^2 = 0.69$	Veg	0.49	**0.04**	**0.04**	1.05	Veg	1.09	**0.04**	**0.04**	1.05
	Intercept	0.59	**2.0E-17**			Intercept	−0.53	**1.7E-10**		
	Price	−0.19	**2.5E-06**	**2.5E-06**	1.00	Price	−0.40	**3.5E-06**	**3.5E-06**	1.00
CVRE $R^2 = 0.72$	Veg	−0.62	0.18	0.26	1.02	Veg	−1.79	0.08	0.12	1.02
$R^2 = 0.71$	SLP	8.5E-03	0.12	0.12	1.02	SLP	0.02	0.11	0.11	1.02
	Intercept	0.53	0.65			Intercept	−0.73	**4.3E-04**		
CVRN $R^2 = 0.40$	Price	−2.38	0.17	0.17	1.00	Price	−0.52	0.07	0.07	—
$R^2 = 0.17$	Veg	−86.59	**2.9E-03**	**2.9E-03**	1.00					

Note: All variables were calculated from microtopographic data of areas of the plot surface belonging to the channel network. CAE and CAD are areal extents (in m^2) of erosion and deposition; CVE, CVD are volumes (in m^3) of erosion and deposition and CVN is the net volume (in m^3) change (Erosion − Deposition); CZE and CZD are average depths (in meters) of erosion and deposition; CAR, is the area-based ratio of channel over total plot area; CVRE is the volume-based ratio of channel erosion over total plot erosion; CVRN is the volume-based ratio of net volume change in channels with respect to the entire plot.

wide equivalents TZE and TZD, the R^2 of the regression and the conclusions remain unchanged, suggesting that processes occurring within the channel network are as informative as plot-wide processes in explaining sediment concentration.

The spatial extent of deposition in channels CAD was mildly non-linear and showed a significant control of discharge and slope. These two factors enhance detachment and transport efficiency and thus reduced the likelihood of within-channel deposition. CVD and CZD showed similar response as TVD and TZD with vegetation controlling deposition volumes and combining with discharge in the control of deposition depth. Again here, slope had a negative effect (significant at 10% confidence level) on deposition volume CVD.

The net volume change within the channel network CVN was significantly lower at Price ($-0.96\,m^3$) and was increased by both discharge and slope. The crisper response of log (CVN) to SLP compared to that of CVE and CVD with this explanatory variable suggest the existence of a transport equilibrium in the channel network whereby excess detachment might be compensated by deposition, i.e. transport capacity.

CAR which can be interpreted as the area-based probability of flow concentration was significantly lower at Price and a positive function of discharge and vegetation. Here again, steeper slopes and higher vegetation cover at Ferron were associated with the development of rills and increased hillslope fragmentation. This is further confirmed by the significantly lower CVRE values at Price, suggesting higher energy expenditure on concentrated flow detachment processes at Ferron. It is important to also note that while vegetation promotes hillslope fragmentation, its positive effect on deposition was associated

Copyright © 2016 John Wiley & Sons, Ltd.

Table IV. Multiple regression analysis on channel expansion metrics.

	Original					Log-transformed				
Explained variable	Explanatory variables	Coef.	Coef. *p*-value	ANOVA *p*-value	VIF	Explanatory variables	Coef.	Coef. *p*-value	ANOVA *p*-value	VIF
	Intercept	0.16	**1.1E-05**			Intercept	−1.64	**6.4E-15**		
	Price	0.10	**4.7E-04**	**7.1E-04**	1.02	Price	0.37	**3.2E-03**	**3.2E-03**	1.00
	Q	4.8E-04	0.11	0.16	1.04	Rdur	2.4E-04	0.16	0.14	1.00
α $R^2 = 0.61$	Rdur	5.4E-05	0.12	0.10	1.02	SLP	−0.04	0.05	0.05	1.00
$R^2 = 0.49$	SLP	−0.01	**0.02**	**0.02**	1.00					
α' $R^2 = 0.25$	Intercept	−0.98	**0.03**			Intercept	−1.21	**8.9E-05**		
$R^2 = 0.26$	*Q*	0.01	**0.02**	**0.02**	—	*SLP*	−0.22	**0.03**	**0.03**	—
	Intercept	0.23	**2.6E-04**			Intercept	−1.32	**1.1E-10**		
*CAE*xy $R^2 = 0.59$	Price	0.16	**1.2E-03**	**4.4E-03**	1.02	Price	0.34	**1.2E-03**	**4.2E-03**	1.02
$R^2 = 0.59$	*Q*	2.3E-03	**4.0E-04**	**4.0E-04**	1.02	*Q*	5.0E-03	**3.8E-04**	**3.8E-04**	1.02
	Intercept	−1.1E-03	0.32			Intercept	−7.25	**1.5E-21**		
*CVE*xy $R^2 = 0.60$	*Q*	7.3E-05	**1.3E-05**	**1.3E-05**	—	*Q*	0.02	**3.6E-09**	**4.7E-09**	1.02
$R^2 = 0.83$						*Rdur*	4.2E-04	0.08	0.08	1.02
	Intercept	2.0E-03	0.26			Intercept	−5.92	**1.2E-19**		
	Price	−3.6E-03	**0.02**	**2.8E-03**	1.02	Price	−0.36	**0.01**	**5.9E-04**	1.02
*CZE*xy $R^2 = 0.72$	*Q*	1.1E-04	**7.5E-06**	**9.8E-06**	1.04	*Q*	0.01	**2.5E-08**	**3.3E-08**	1.04
$R^2 = 0.84$	Rdur	2.7E-06	0.20	0.20	1.02	Rdur	3.3E-04	0.09	0.09	1.02
	Intercept	0.13	**1.7E-06**			Intercept	−1.69	**4.5E-05**		
	Price	−0.03	0.06	0.17	1.02	Price	−0.77	**9.2E-03**	0.05	1.02
*CAD*xy $R^2 = 0.60$	*Q*	−9.4E-04	**2.7E-04**	**1.0E-04**	1.07	*Q*	−0.02	**7.9E-06**	**2.7E-06**	1.07
$R^2 = 0.73$	Veg	0.37	0.16	0.16	1.05	Veg	7.02	0.11	0.11	1.05
	Intercept	3.5E-04	**5.1E-05**			Intercept	−7.65	**1.1E-12**		
	Q	−3.0E-06	**2.3E-03**	**2.3E-03**	1.00	Price	−0.65	0.11	0.31	1.02
*CVD*xy $R^2 = 0.43$	SLP	2.1E-05	0.10	0.10	1.00	*Q*	−0.02	**1.6E-04**	**1.7E-04**	1.02
$R^2 = 0.58$						SLP	0.14	0.07	0.07	1.00
	Intercept	2.9E-03	**6.5E-05**			Intercept	−6.06	**1.6E-24**		
*CZD*xy $R^2 = 0.13$	SLP	3.7E-04	0.09	0.09	—	SLP	0.09	**0.03**	**0.03**	—
$R^2 = 0.22$										
	Intercept	−1.4E-03	0.19			Intercept	−7.96	**5.5E-16**		
*CVN*xy $R^2 = 0.62$	*Q*	7.6E-05	**7.8E-06**	**7.8E-06**	—	*Q*	0.03	**7.2E-06**	**7.2E-06**	—
$R^2 = 0.62$										
	Intercept	1.55	**9.5E-07**			Intercept	0.34	**0.03**		
	Q	0.01	**6.7E-04**	**2.5E-04**	1.05	*Q*	6.2E-03	**2.2E-03**	**2.2E-03**	—
*CAE*z $R^2 = 0.58$	Veg	−5.11	0.13	0.23	1.07					
$R^2 = 0.37$	SLP	0.08	0.05	0.05	1.02					
	Intercept	2.1E-03	0.47			Intercept	−5.66	**6.7E-19**		
	Price	−9.0E-03	**1.2E-03**	**1.1E-04**	1.02	Price	−0.53	**8.2E-04**	**3.2E-05**	1.02
*CVE*z $R^2 = 0.79$	*Q*	2.2E-04	**6.2E-07**	**6.2E-07**	1.02	*Q*	0.02	**2.9E-09**	**2.9E-09**	1.02
$R^2 = 0.88$						SLP	0.06	**0.02**	**0.02**	1.00
	Intercept	1.89	**1.4E-08**			Intercept	0.65	**4.8E-04**		
	Q	−9.1E-03	**1.7E-03**	**6.4E-04**	1.05	*Q*	−7.8E-03	**6.5E-04**	**1.9E-04**	1.05
*CAD*z $R^2 = 0.54$	Veg	4.86	0.12	0.20	1.07	Veg	4.65	0.06	0.11	1.07
$R^2 = 0.61$	SLP	−0.07	0.06	0.06	1.02	SLP	−0.06	**0.04**	**0.04**	1.02
	Intercept	4.6E-03	**3.6E-08**			Intercept	−5.57	**1.0E-22**		
	Rdur	2.6E-06	0.10	0.09	1.00	Veg	10.13	**6.8E-03**	**0.01**	1.02
*CVD*z $R^2 = 0.36$	Veg	0.04	**0.04**	0.06	1.02	SLP	−0.09	**0.04**	**0.04**	1.02
$R^2 = 0.38$	SLP	−3.5E-04	0.08	0.08	1.02					
	Intercept	2.6E-03	**3.0E-03**			Intercept	−5.94	**8.2E-24**		
	Price	−3.5E-03	**2.9E-05**	**2.9E-06**	1.02	Price	−0.65	**1.3E-08**	**7.9E-10**	1.02
	Q	6.0E-05	**5.0E-07**	**5.0E-07**	1.02	*Q*	0.01	**1.1E-10**	**1.3E-10**	1.04
*CZE*z $R^2 = 0.82$						Rdur	2.3E-04	**0.03**	**0.04**	1.02
$R^2 = 0.95$						SLP	0.03	**0.01**	**0.01**	1.00
	Intercept	1.6E-03	**1.4E-03**			Intercept	−6.24	**3.2E-21**		
	Q	3.0E-05	**2.0E-05**	**9.4E-05**	1.07	*Q*	8.1E-03	**8.7E-05**	**3.7E-04**	1.07
	Rdur	1.0E-06	0.10	0.11	1.02	Rdur	2.9E-04	0.13	0.14	1.02
*CZD*z $R^2 = 0.68$	Veg	0.02	**5.7E-03**	**8.4E-03**	1.07	Veg	5.21	**0.01**	**0.01**	1.05
$R^2 = 0.60$	SLP	−1.0E-04	0.19	0.19	1.03					

Note: Variables in the first column were calculated by isolating areas corresponding to lateral channel network expansion (variables ending in *xy*) from those that underwent vertical changes as the result of rainfall (variable ending in *z*). α and α' are the proportion of volume change associated with channel expansion. α was calculated based on erosion volumes while α' was calculated from net volume changes. CAE*xy*, CAD*xy*, CAE*z* and CAD*z* are areal extents (in m^2) of erosion and deposition; CVE*xy*, CVD*xy*, CVE*z* and CVD*z* are volumes (in m^3) of erosion and deposition and CVN*xy* is the net volume (in m^3) change (Erosion − Deposition); CZE*xy*, CZD*xy*, CZE*z*, and CZD*z* are average depths (in meters) of erosion and deposition.

Copyright © 2016 John Wiley & Sons, Ltd.

with a lowered ratio of channel to plot-wide net erosion CVRN. When the site factor was replaced by slope in the CAR multiple regression and the vegetation variable decoupled from slope [by using the residuals of $\mathrm{Veg} = f(\mathrm{SLP}) = 8.6 \times 10^{-3}\mathrm{SLP} + 0.045$], the following equation was obtained with all coefficients significant:

$$CAR = 1.3 \cdot 10^{-3} \times SLP + 5.2 \cdot 10^{-4} \times Q + 0.43 \times Veg + 0.31, R^2 = 0.69 \tag{20}$$

In addition, the analysis of variance performed on this model showed statistical significance of all variables at 5% confidence level.

Variables and metrics characterizing changes to the channel network are summarized in Table IV. The proportion of energy expenditure on lateral channel growth α was 10% higher at Price than it was at Ferron. The results obtained on CAE*xy*, CVE*xy* and CZE*xy* suggest that channels grew wider at Price but remained shallower than those at Ferron. The steeper slopes at this site increased shear stress on channel bottom, leading to increased scouring and channel deepening. This finding is further supported by the significant negative effect of SLP on α and positive on log(CVE*z*). Partitioning concentrated flow detachment energy into that acting on channel walls (CVE*xy*) and that acting on channel bottoms (CVE*z*) clearly shows the dependence of the former on discharge alone while the latter was controlled by both discharge and slope. Other factors such as soil intrinsic properties (texture, erodibility, etc.) also control channel network geometry (e.g. Gilley *et al*., 1990) but were not the object of this study.

When deposition was accounted in the estimation of energy expenditure (α'), the R^2 of the multiple regression decreased by 36 points compared to that obtained for α but slope persisted as a significant explanatory variable. Deposition within the newly colonized channel areas (zone of lateral expansion CAD*xy*) was less likely at Price than it was at Ferron. The higher vegetation cover at Ferron increased the likelihood of deposition in general at this site. Discharge negatively controlled CAD*xy* and CVD*xy* as a result of increased transport efficiency. This result differs from what was observed for CVD, which was only dependent on vegetation, suggesting that discharge essentially controlled processes (both erosion and deposition) occurring laterally within the channel. The amount of deposition occurring in the pre-existing channel network CVD*z* was a function of vegetation and slope. As observed with CVD, the form roughness imparted to the hillslope by vegetation was associated with concentrated flow disruption and opportunity for deposition to occur. In addition, the results on log(CVD*z*) suggest a significant control of slope on transport efficiency. The positive effect of discharge on CZD*z* as in the case of CZD and TZD can be explained by the spatial constraint theory described earlier.

In summary, erosivity which in this study is represented by runoff discharge drives detachment and transport processes while factors controlling surface roughness such as vegetation oppose transport of the detached particles (Figure 10). This is well illustrated in the positive response of the net erosion volume (TVN and CVN), with Q and a decreasing effect of Veg on TVN and CVRN. Furthermore land topography (SLP) likely controlled detachment (positive significant CVN–SLP relationship) as well as transport efficiency (negative significant at 20% of TDR–SLP coefficient in Table II) but these effects were possibly muffled by the dominance of Q on transport processes.

Discussions

Insight into concentrated flow erosion processes

Concentrated flow erosion is a complex process because rill networks have a function of sediment and runoff production and storage and also serve as transport vessels of these resources off-site. Both functions of runoff and sediment production and transport are intricately coupled and traditionally assumed to be controlled by rill flow hydraulics. The key to accurate concentrated flow erosion has therefore been that of adequate prediction of hydraulic parameters. A great deal of

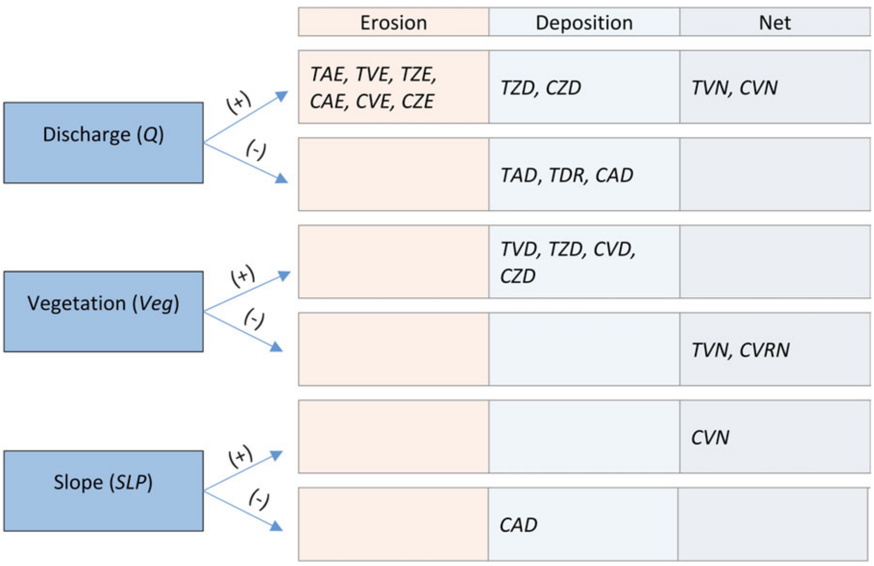

Figure 10. Summary of statistically significant relationships between discharge Q, vegetation Veg and slope SLP and key surface change metrics. Surface change metrics corresponding to plot-wide surface change metrics begin with the letter 'T' while those corresponding to channel processes begin with letter 'C'. TAE, TAD, CAE and CAD are plot-wide and channel areal extents (in m^2) of erosion and deposition; TVE, TVD, CVE and CVD are volumes (in m^3) of erosion and deposition and TVN and CVN are the net volume (in m^3) change (Erosion − Deposition); TZE, TZD CZE and CZD are average depths (in meters) of erosion and deposition; TDR is the ratio of deposition over erosion volumes (TVD/TVE). CVRN is the volume-based ratio of net volume change in channels with respect to the entire plot. The symbols (+) and (−) represent respectively positive and negative relationships. [Colour figure can be viewed at wileyonlinelibrary.com]

Copyright © 2016 John Wiley & Sons, Ltd.

research efforts have been invested into relating rill detachment rate to flow hydraulic parameters such as average shear stress (e.g. Lyle and Smerdon, 1965; Torri *et al.*, 1987; Ghebreiyessus *et al.*, 1994; Nearing *et al.*, 1997), stream power (e.g. Bagnold, 1977; Nearing *et al.*, 1997; Zhang *et al.*, 2003), and effective stream power (e.g. Bagnold, 1980). Performance tests of these hydraulic parameters at predicting rill detachment rate in various experimental conditions (Al-Hamdan *et al.*, 2012; Wirtz *et al.*, 2013) resulted in no single parameter consistently best-fitting observed detachment rates, although Nearing *et al.* (1997) and Al-Hamdan *et al.* (2012) found that the stream power performed well with rangeland erosion data. Wirtz *et al.* (2013) attributed discrepancies between observed and predicted erosions to the inherent emphasis of most hydraulic parameters on fluvial processes incising channel bottoms while diffusive processes such as headcut retreat and bank erosion make up a non-negligible portion of rill detachment. In this study, we found that channel lateral expansion (e.g. CVE*xy*) was primarily controlled by runoff discharge while forces acting on channel bottom (e.g. CVE*z*) were a result of a combined effect of discharge and slope. Our results also show that when CVE*xy* and CVE*z* were combined into CVE, the significance of the slope effect was lessened. Most rill hydraulic parameters are derived from a combination of runoff discharge and slope. Relating these hydraulic parameters to total concentrated flow erosion (CVE as a proxy in this paper), might result in poor prediction performance. In fact in our study, when discharge and slope were replaced with stream power $\omega = Q \times \mathrm{SLP}$, then R^2 values were 0.85 and 0.79 for CVE and log(CVE), 0.57 and 0.60 for CVE*xy* and log(CVE*xy*) and 0.92 and 0.83 for CVE*z* and log(CVE*z*). The use of the stream power improved the non-linearity observed in CVE and CVE*z* (Tables III and IV). In addition, compared to R^2 values shown in Tables III and IV, there was a substantial improvement in R^2 with the use of ω on CVE*z* and mild improvement on CVE while the explained CVE*xy* variance was reduced. This finding is consistent with Wirtz *et al.*'s (2013) conclusion that concentrated flow erosion is a sum of diffusive and fluvial processes that are not fully captured by most hydraulic parameters.

The area-based ratio of concentrated flow process over plot-wide process CAR can be interpreted as the probability of flow concentration. In this study, we found that CAR was increased by slope, discharge and vegetation cover (Equation (20)). This area-based probability of flow concentration assumes that an initial channel network controlled by hillslope topography (SLP), biotic factors (Veg) and recent and/or long-term erosion history was altered during the simulated rainfall event with erosivity determined by Q and SLP. This approach differs from that proposed in Al-Hamdan *et al.* (2013) which estimates the probability that runoff discharge will concentrate during an event. Al-Hamdan *et al.*'s (2013) approach was developed from non-saline soils which might behave differently than soils at Price and Ferron. In addition, Al-Hamdan *et al.* (2013) defined concentrated flow erosion based on hydraulic characteristics of runoff which contrasts with the microtopography-based definition in our study. Nevertheless, both approaches agree on the positive effects of slope and discharge on the likelihood of flow concentration. Note however that in Al-Hamdan *et al.*'s (2013) equation, the proportion of bare ground had a facilitative effect on flow concentration likelihood while in our study, vegetation (inversely related to bare ground) promoted flow concentration ratio CAR. These seemingly contradictory results might be providing us with a better understanding of the role of vegetation in controlling concentrated flow processes. The positive effect of vegetation on CAR was the result of CAE + CAD being independent of vegetation while the presence of vegetation reduced the effective plot area TAE + TAD. This result indicates that vegetation might structure runoff into multiple flow paths so that the extent of the flow network is in equilibrium with discharge. However, as indicated by the negative effects of vegetation on the volume-based ratios CVRE and CVRN, energy expenditure on concentrated flow erosion might be lessened by an increase in vegetation, potentially leading to smaller hydraulic radii in each flow path and lower probability of hydraulics-based flow-concentration used in Al-Hamdan *et al.* (2013).

Management implications

The ultimate goal of this study was to improve understanding of salt mobilization and transport in the UCRB and develop effective mitigation strategies that would reduce salt delivery to the Colorado River. The Colorado River and its tributaries provide water to about 36 million people and irrigation water to nearly six million acres of land in the United States and Mexico (Bureau of Reclamation, 2013). Damages within the United States from dissolved solids in the Colorado River have been estimated to $295 million per year (Bureau of Reclamation, 2013). Salinity-control efforts have largely focused on reducing anthropogenic sources of dissolved-solids especially irrigation of agricultural lands while nearly half of the salinity concentration in the river system comes from natural sources (saline springs, erosion of saline geologic formations and runoff) (Kenney et al., 2009). This suggests a significant potential to further reduce dissolved-solids loading to the Colorado River through land- and water-management activities on natural rangelands.

Soils at both Price and Ferron are in the Mancos Shale geologic formation which is well known to be one the major contributor to surface water salinity (e.g. Tuttle and Grauch, 2009) and understanding the salt pickup and transport processes at these sites will help in the development of effective mitigation strategies. A basic premise in developing salinity reduction strategies in these saline rangelands has been to control soil erosion and transport due to the proven linkage between runoff sediment concentration and total dissolved solids (Hawkins et al., 1977). In our study, parsing sediment transport processes into their elementary components with the 3D information provides us with a more detailed understanding of processes controlling salt pickup and transport.

Equation (19) suggests that to reduce sediment and thus salt concentration, one can act upon discharge or promote deposition. Since in this study, runoff discharge reflects erosivity, one mitigation strategy could aim to reduce soil and salt pickup through increasing vegetation cover. However, the arid conditions (<250 mm/yr) combined with the high soil salinity prevailing at these sites might make it difficult to substantially increase vegetation cover to achieve targeted detachment reduction. In addition, chemical soil stabilization techniques such as the use of polyacrylamide (e.g. Aase *et al.*, 1998; Shainberg *et al.*, 1994; Newhall *et al.*, 2004) might prove onerous considering the large spatial scale of the problem. Our study suggests that a more effective approach might be to target transport and deposition processes to control sediment concentration and salt load. We showed that the form roughness imparted to the soil surface by vegetation was responsible for reduced transport efficiency and created opportunities for deposition. More success might be achieved by strategically creating zones of increased roughness along hillslope channel networks where deposition can occur. One possible approach could be the introduction of salt-tolerant herbaceous vegetation at regular intervals along hillslope flow concentration pathways.

Copyright © 2016 John Wiley & Sons, Ltd.

Conclusions

The 3D surface change metrics developed in this study were successful at capturing the expression of various erosion and sediment transport processes and how these processes were influenced by hydrologic input and biotic and abiotic land surface characteristics. We found in this study that cumulative runoff performed better than cumulative soil loss at predicting plot-wide 3D erosion volumes, an indication that runoff may be responsible for hydrodynamic changes to soil surface microtopography in addition to detachment and transport of soil particles. Plot-wide deposition values were poorly correlated with soil loss and discharge but were primarily controlled by vegetation with a mild influence of slope. Our results suggest that erosivity drives detachment and transport processes while factors controlling surface roughness such as vegetation promoted deposition, and these patterns were accentuated within the channel network.

Across the two sites studied, the extent of the channel network was primarily controlled by discharge, with vegetation structuring runoff into flow paths to maintain a channel network extent in equilibrium with discharge. Concentrated flow erosion volumes and average depths were lower at Price than they were at Ferron, due to the lower slopes at the former site. Deposition volume in channels was also a function of vegetation cover with average depth of deposition increased when area available for deposition was reduced by discharge.

When concentrated flow detachment energy was parsed into that acting on channel walls and that acting on channel bottoms, the former was dependent on discharge alone while the latter was controlled by both discharge and slope. This finding has significant implication in concentrated flow erosion modeling.

This study showed that significant improvement to erosion and sediment transport models can be achieved by augmenting traditional soil loss and runoff measurement with 3D surface change information. It is often the case that environments where these 3D reconstruction techniques perform well are also susceptible to soil erosion and sediment transport. Knowledge gained from this improved understanding of sediment transport processes will help design effective management and mitigation strategies that target specific physical processes to achieve desired outcomes. In this study, we have found for example that the key to runoff soil and salt load reduction likely lies in promoting deposition by creating zones of increased roughness along concentrated flow pathways.

Acknowledgements—This study was funded by the USDI-Bureau of Reclamation, USDI-Bureau of Land Management, the USDA Agricultural Research Service (Cooperative Agreement 59-5370-3-001), in collaboration with the Desert Research Institute and the University of Nevada, Reno of the Nevada System of Higher Education. USDA is an equal opportunity provider and employer. Mention of a proprietary product does not constitute a guarantee or warranty of the product by USDA or the authors, and it does not imply its approval to the exclusion of the other products that also may be suitable.

References

Aase JK, Bjorneberg DL, Sojka RE. 1998. Sprinkler irrigation runoff and erosion control with polyacrylamide – laboratory tests. *Soil Science Society of America Journal* **62**: 1681–1687.

Agisoft LLC. 2013. *Agisoft Photoscan Professional Edition*. Agisoft LLC: St Petersburg.

Al-Hamdan OZ, Pierson FB, Nearing MA, Williams CJ, Stone JJ, Kormos PR, Boll J, Weltz MA. 2012. Concentrated flow erodibility for physically based erosion models: temporal variability in disturbed and undisturbed rangelands. *Water Resources Research*: 48. DOI:10.1029/2011wr011464.

Al-Hamdan OZ, Pierson FB, Nearing MA, Williams CJ, Stone JJ, Kormos PR, Boll J, Weltz MA. 2013. Risk assessment of erosion from concentrated flow on rangelands using overland flow distribution and shear stress partitioning. *Transactions of the ASABE* **56**: 539–548.

Bagnold RA. 1977. Bed load transport by natural rivers. *Water Resources Research* **13**: 303–312. DOI:10.1029/WR013i002p00303.

Bagnold RA. 1980. An empirical correlation of bedload transport rates in flumes and natural rivers. *Proceedings of the Royal Society London Series A – Mathematical, Physical and Enginnering Science* **372**: 453–473. DOI:10.1098/rspa.1980.0122.

Bonnin GM, Martin D, Lin B, Parzybok T, Yekta M, Riley D. 2006. *Precipitation-frequency Atlas of the United States*, NOAA atlas 14. National Oceanic and Atmospheric Administration: Washington, DC.

Bowles DS, Nezafati H, Bhasker RK, Riley JP, Wagenet RJ. 1982. *Salt Loading from Efflorescence and Suspended Sediments in the Price River Basin*, Water Resources Planning Series. Utah Water Research Laboratory, Utah State University: Logan, UT; 142.

Bracken LJ, Croke J. 2007. The concept of hydrological connectivity and its contribution to understanding runoff-dominated geomorphic systems. *Hydrological Processes* **21**: 1749–1763. DOI:10.1002/hyp.6313.

Bureau of Reclamation. 2013. *Quality of Water Colorado River Basin Progress Report No. 24 Managing Water in the West*. United States Department of the Interior: Washington, DC; 130.

Castillo C, Perez R, James MR, Quinton JN, Taguas EV, Gomez JA. 2012. Comparing the accuracy of several field methods for measuring gully erosion. *Soil Science Society of America Journal* **76**: 1319–1332. DOI:10.2136/sssaj2011.0390.

Evironmental Systems Research Institute (ESRI). 2011. *Arcgis Desktop Release 10*. ESRI: Redlands, CA.

General Public Licence. 2014. *Cloudcompare v2.5*. General Public Licence.

Ghebreiyessus YT, Gantzer CJ, Alberts EE. 1994. Soil erosion by concentrated flow: shear stress and bulk density. *Transactions of the ASAE* **37**: 1791–1797.

Gilley JE, Kottwitz ER, Simanton JR. 1990. Hydraulic characteristics of rills. *Transactions of the ASAE* **33**: 1900–1906.

Hawkins RH, Gifford GF, Jurinak JJ. 1977. *Effects of Land Processes on the Salinity of the Upper Colorado River Basin: Final Project Report*. Utah State University: Logan, UT; 196.

Hyun-Chong C, Srinivasan S, Sedighi A, Slatton KC. 2006. Extraction of stream channels in high-resolution digital terrain images using morphology. *Proceedings, Geoscience and Remote Sensing Symposium, 2006. IGARSS 2006. IEEE International Conference*, 31 July–4 August; 1078–1081.

James MR, Robson S. 2012. Straightforward reconstruction of 3d surfaces and topography with a camera: Accuracy and geoscience application. *Journal of Geophysical Research: Earth Surface* **117**. DOI:10.1029/2011JF002289.

Kenney TA, Gerner SJ, Buto SG, Spangler LE. 2009. *Spatially Referenced Statistical Assessment of Dissolved-solids Load Sources and Transport in Streams of the Upper Colorado River Basin*, USGS Scientific Investigations Report. US Geological Survey: Reston, VA; 50.

Lyle W, Smerdon E. 1965. Relation of compaction and other soil properties to erosion resistance of soils. *Transactions of the ASAE* **8**: 419–422.

Nearing M, Norton L, Bulgakov D, Larionov G, West L, Dontsova K. 1997. Hydraulics and erosion in eroding rills. *Water Resources Research* **33**: 865–876.

Nearing MA, Wei H, Stone JJ, Pierson FB, Spaeth KE, Weltz MA, Flanagan DC, Hernandez M. 2011. A rangeland hydrology and erosion model. *Transactions of the ASABE* **54**: 901–908.

Newhall RL, Monaco TA, Horton WH, Harrison RD, Page RJ. 2004. Rehabilitating salt-desert ecosystems following wildfire and wind erosion. *Rangelands* **26**: 3–7. DOI:10.2111/1551-501X(2004)26[3:RSEFWA]2.0.CO;2.

Nichols MH, Nearing MA, Polyakov VO, Stone JJ. 2013. A sediment budget for a small semiarid watershed in southeastern arizona, USA. *Geomorphology* **180**: 137–145. DOI:10.1016/j.geomorph.2012.10.002.

Copyright © 2016 John Wiley & Sons, Ltd.

Nouwakpo SK, James MR, Weltz MA, Huang C-H, Chagas I, Lima L. 2014. Evaluation of structure from motion for soil microtopography measurement. *The Photogrammetric Record* **29**: 297–316. DOI:10.1111/phor.12072.

Nouwakpo SK, Weltz M, Champa T, Fisher J. 2016a. Performance of the rangeland hydrology and erosion model for runoff and erosion assessment on a semi-arid reclaimed construction site. *Journal of Soil and Water Conservation* **71**(3): 220–236.

Nouwakpo SK, Weltz MA, McGwire K. 2016b. Assessing the performance of structure-from-motion photogrammetry and terrestrial lidar for reconstructing soil surface microtopography of naturally vegetated plots. *Earth Surface Processes and Landforms* **41**(3): 308–322. DOI:10.1002/esp.3787.

Paige GB, Stone JJ, Smith JR, Kennedy JR. 2004. The walnut gulch rainfall simulator: a computer-controlled variable intensity rainfall simulator. *Applied Engineering in Agriculture* **20**: 25–31.

Pierson FB, Williams CJ, Hardegree SP, Weltz MA, Stone JJ, Clark PE. 2011. Fire, plant invasions, and erosion events on western rangelands. *Rangeland Ecology and Management* **64**: 439–449. DOI:10.2111/REM-D-09-00147.1.

R Development Core Team. 2015. *R: A Language and Environment for Statistical Computing*. R Foundation for Statistical Computing: Vienna.

Riley JP, Bowles DS, Chadwick DG, Grenney WJ. 1979. Preliminary identification of price river basin salt pickup and transport processes. *JAWRA Journal of the American Water Resources Association* **15**: 984–995. DOI:10.1111/j.1752-1688.1979.tb01077.x.

Riley JP, Chadwick DG, Dixon LS, James LD, Grenney WJ. 1982. *Salt Uptake in Natural Channels Traversing Mancos Shales in the Price River Basin, Utah*. US Geological Survey: Reston, VA.

Rodriguez F, Maire E, Courjault-Radé P, Darrozes J. 2002. The black top hat function applied to a dem: A tool to estimate recent incision in a mountainous watershed (estibère watershed, central pyrenees). *Geophysical Research Letters* **29**: 9-1–9-4. DOI:10.1029/2001GL014412.

Schwanghart W, Groom G, Kuhn NJ, Heckrath G. 2013. Flow network derivation from a high resolution dem in a low relief, agrarian landscape. *Earth Surface Processes and Landforms* **38**: 1576–1586. DOI:10.1002/esp.3452.

Shainberg I, Laflen JM, Bradford JM, Norton LD. 1994. Hydraulic flow and water quality characteristics in rill erosion. *Soil Science Society of America Journal* **58**: 1007–1012.

Torri D, Sfalanga M, Chisci G. 1987. Threshold conditions for incipient rilling. *Catena* **8**(Supplement): 97–105.

Tuttle ML, Grauch RI. 2009. *Salinization of the Upper Colorado River—Fingerprinting Geologic Salt Sources*, USGS Scientific Investigations Report. US Geological Survey, Reston, VA; 62.

Wainwright J, Parsons AJ, Abrahams AD. 2000. Plot-scale studies of vegetation, overland flow and erosion interactions: Case studies from arizona and new mexico. *Hydrological Processes* **14**: 2921–2943.

Western Regional Climate Center (WRCC). 2015. *Cooperative Climatological Data Summaries*. WRCC: Sun Valley, NV.

Westoby MJ, Brasington J, Glasser NF, Hambrey MJ, Reynolds JM. 2012. 'Structure-from-motion' photogrammetry: a low-cost, effective tool for geoscience applications. *Geomorphology* **179**: 300–314. DOI:10.1016/j.geomorph.2012.08.021.

Williams CJ, Pierson FB, Robichaud PR, Boll J. 2014. Hydrologic and erosion responses to wildfire along the rangeland-xeric forest continuum in the western us: a review and model of hydrologic vulnerability. *International Journal of Wildland Fire* **23**: 155–172. DOI:10.1071/wf12161.

Williams CJ, Pierson FB, Robichaud PR, Al-Hamdan OZ, Boll J, Strand EK. 2016. Structural and functional connectivity as a driver of hillslope erosion following disturbance. *International Journal of Wildland Fire* **25**: 306–321. DOI:http://dx.doi.org.unr.idm.oclc.org/10.1071/WF14114.

Wirtz S, Seeger M, Zell A, Wagner C, Wagner JF, Ries JB. 2013. Applicability of different hydraulic parameters to describe soil detachment in eroding rills. *PLoS One* **8**(5): e64861. DOI:10.1371/journal.pone.0064861.

Zhang GH, Liu BY, Liu GB, He XW, Nearing MA. 2003. Detachment of undisturbed soil by shallow flow. *Soil Science Society of America Journal* **67**: 713–719.

Supporting Information

Additional supporting information may be found in the online version of this article at the publisher's web site.

Copyright © 2016 John Wiley & Sons, Ltd.